Available online at www.sciencedirect.com

ScienceDirect

Geochimica et Cosmochimica Acta 254 (2019) 54–66

Geochimica et Cosmochimica Acta

www.elsevier.com/locate/gca

The phase diagram of the Fe-P binary system at 3 GPa and implications for phosphorus in the lunar core

Yuan Yin [a,b], Zeming Li [a,b], Shuangmeng Zhai [a,*]

[a] Key Laboratory of High-temperature and High-pressure Study of the Earth's Interior, Institute of Geochemistry, Chinese Academy of Sciences, Guiyang 550081, China

[b] University of Chinese Academy of Sciences, Beijing 100049, China

Received 8 May 2018; accepted in revised form 28 March 2019; available online 5 April 2019

Abstract

Phosphorus is a potential candidate in the metallic core of the Moon. The phase diagram of the Fe-P binary system was investigated at the pressure of 3 GPa and temperatures of up to 1600 °C. Up to 3.0 wt% and 10.4 wt% phosphorus can dissolve in the solid iron and liquid Fe-P phases at 1100 °C and 3 GPa, respectively. The eutectic temperature on the iron-rich side was determined as 1085 °C at 3 GPa. The solubility of phosphorus in the iron decreases from ~1.4 wt% at 1100 °C to ~0.7 wt% at 1500 °C and 3 GPa. Structure of the solid iron in the quenched sample is the body-center cubic, corresponding to α-Fe phase. Extending the phosphorus solubility in the solid iron to the present lunar core conditions yields a maximum phosphorus concentration in a fully crystallized iron core of 0.85 ± 0.15 wt%. If there are Ni and C in the core, the value would be depressed to 0.4 ± 0.1 wt%. In addition, based on a simple siderophile mass balance between the bulk Moon (BM) and bulk silicate Moon (BSM) and a modeled phosphorus partition coefficient, $D_{\text{P-Moon}}^{\text{core/mantle}}$ (40–200) for the lunar magma ocean, a bulk silicate Earth-like P content (82 ± 8 ppm) in the initial Moon yields a lunar core with <0.3 wt% P. Some other potential light elements such as S and C could reduce the P content in the lunar core. Furthermore, the partition coefficient of phosphorus in the iron and liquid melt ($D_{\text{P}}^{\text{SM/LM}}$) was found to be 0.10 ± 0.03 at 3 GPa. Taking the sulfur into account, the $D_{\text{P}}^{\text{SM/LM}}$ increase to 0.18 ± 0.02 at 5 GPa in the S-rich liquid metal (~8 wt%). In the case of a solid lunar inner core and S-bearing liquid outer core, their P contents were assessed to be less than 0.09 ± 0.01 wt% and 0.51 ± 0.01 wt%, respectively, when the lunar core's storage of P is <0.3 wt%. The moderate phosphorus solubility in the solid iron, combined with the assumption of abundant phosphorus in the bulk Moon, indicates that the phosphorus concentration in the lunar core could higher than previously thought.

© 2019 Elsevier Ltd. All rights reserved.

Keywords: Fe-P binary system; High pressure; Phase diagram; Lunar core

1. INTRODUCTION

Based on the geophysical evidence from lunar seismology (Lognonné and Johnson, 2007; Weber et al., 2011) and laser ranging (Williams et al., 2001), Moon is supposed to have a small metallic core, even with a solid inner and liquid outer core. Like the chemical composition model for the Earth's core, some light elements, such as carbon and sulfur, are suggested to alloy with iron in the lunar core. To explain geophysical observation, the concentration of sulfur in the lunar outer core has been constrained in different models (Weber et al., 2011 - <6 wt% S; Jing et al., 2014 – 3.6 wt% S; Antonangeli et al., 2015 6–11 wt%; Kuwabara et al., 2016). Models for metal/silicate partitioning of siderophile elements in the lunar magma ocean

* Corresponding author at: Institute of Geochemistry, Chinese Academy of Sciences, Guiyang, Guizhou 550081, China.
E-mail address: zhaishuangmeng@vip.gyig.ac.cn (S. Zhai).

https://doi.org/10.1016/j.gca.2019.03.037
0016-7037/© 2019 Elsevier Ltd. All rights reserved.

(LMO) also support a sulfur-rich core (Rai and van Westrenen, 2014, 6–8 wt% sulfur). However, the sulfur may not be the dominant light element in the lunar core. Steenstra et al. (2017) suggest a carbon-dominant core with 0.6–4.8 wt%, including relative lower sulfur concentration (<0.16 wt%). Recent studies have experimentally determined plausible ranges of S in the bulk silicate Moon which suggest the estimated S concentration in the lunar mantle could not meet the requirement for a lunar core that contains several wt% S (Bombardieri et al., 2005; Ding et al., 2017; Steenstra et al., 2018). According to the phase equilibria experiments on the Fe-Ni-S-C system at the temperature and pressure conditions relevant to the lunar interior, Righter et al. (2017) proposed a low S- and C content core (0.5 wt% C, 0.375 wt% S) which provides a simple heat source and mechanism for a lunar core dynamo (core crystallization). That composition would result in 3.8–11.8 wt% S and 1.7–2.4 wt% C in the fluid outer core with ~1.2 wt% C and ~0.02 wt% S in the solid Fe inner core.

Due to the depletion relative to CI chondrites and bulk silicate Earth (BSE), phosphorus is believed to be enriched in the iron-nickel core of the Moon by the core-mantle differentiation (Righter and Drake, 1996; Righter, 2002). Depending on the P/Nd ratio in meteorites, the phosphorus content in the bulk silicate Moon (C^{P}_{BSM}) was estimated to be 20 ppm, with a phosphorus content of 43 ppm in the bulk Moon (C^{P}_{BM}) (O'Neill, 1991). Approximately 0.1 wt% P may present in the lunar core by the core-mantle differentiation, which means that 55 wt% of the total phosphorus budget is in the core (Drake, 1987; Sha, 2000). Righter (2002) estimated the P concentration in the lunar mantle by different Moon-forming impact models, resulting in 8–56 ppm. However, this value is still in debate according to the theory that the abundance of major elements are same on the Moon and Earth (95 ± 15 ppm P from Ringwood, 1991). In the estimation of the bulk silicate Moon (BSM) by Hauri et al. (2015), 0.0206 wt% P_2O_5, equal to 90 ppm P, is present in the lunar mantle. The bulk silicate Moon enriched in crustal components model (the cBSM model) proposed by Togashi et al. (2017) suggested that up to 0.04 wt% P_2O_5, equal to 174 ppm P, was present in the initial silicate Moon after the giant impact, much higher than the 20 ppm estimated previously by O'Neill (1991). Because of the core-mantle differentiation, the C^{P}_{BSM} is the key that controls the P budget in the lunar core thought the C^{P}_{BSM} is still unclear. In addition, the Fe-P phase diagram may provide valuable information to constrain the concentration of phosphorus in the lunar core.

Saklatwalla (1908) firstly published the phase relationship of the Fe-P system (0–24 wt% P) at ambient pressure conditions. Then Konostantinow (1910) and Haughton (1927) measured the Fe-P binary phase diagram up to 24 and 32 wt% P, respectively. The phase diagram at ambient pressure was reassessed by Zaitsev et al. (1995) using thermodynamic analyses. Stewart and Schmidt (2007) conducted Fe-P-S and Fe-P experiments at 23 GPa using multi-anvil presses. Compared with the value of 2.6 wt% at ambient pressure shown in Fig. 1(a), the solubility of phosphorus in α-Fe increases to 4 wt% at 23 GPa (Fig. 1 (b)). Up to ~ 9 wt% phosphorus is soluble in the Fe-P melt at 1275 °C and 23 GPa (Fig. 1b). Even though the phosphorus solubility in the iron is appreciable, Stewart and Schmidt (2007) considered that phosphorus would not form a distinct phase within terrestrial planet cores due to the expectation of its minor concentration in planetary cores. However, to determine the phosphorus content in the Moon's core, the previous Fe-P phase diagram is insufficient and only contains a few experiment data conducted at 23 GPa (Stewart and Schmidt, 2007), which is inappropriate for the lunar core conditions at 4.5 GPa (core-mantle-boundary) to 5.3 GPa (inner core) (Kuskov and Kronrod, 1998; Garcia et al., 2011). A very recent study investigated the pressure dependence of the liquidus and solidus temperatures on the iron-rich side of the Fe-P binary system by using *in-situ* ultrasonics at 2 and 4 GPa (Chantel et al., 2018). But, they provide little chemical composition information for the Fe-P binary system. Here we investigated the Fe-P phase diagram at 3 GPa and

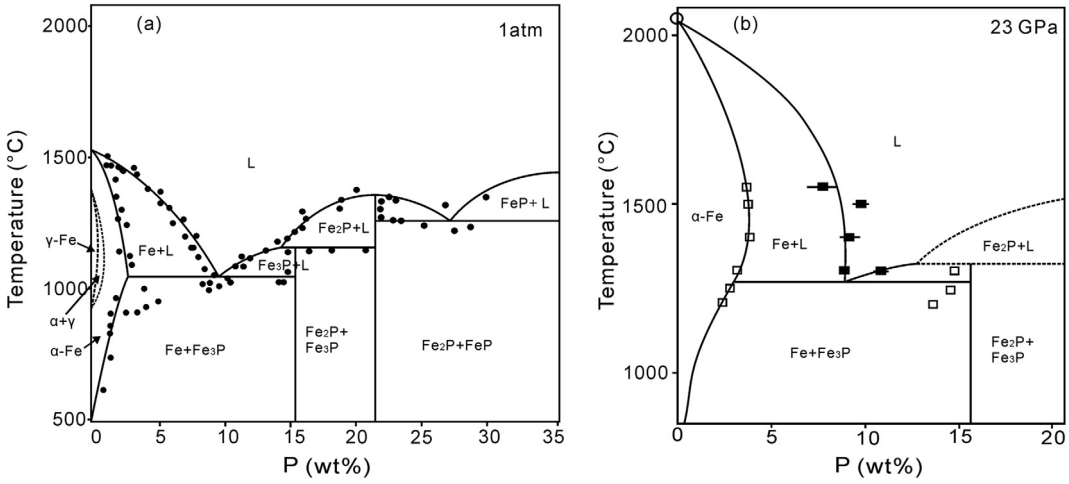

Fig. 1. Fe-P phase diagrams at ambient pressure (a) (Baker, 1992; Zaitsev et al., 1995) and 23 GPa (b) (Stewart and Schmidt, 2007). Circle and square markers represent the experimental data.

determined the phosphorus solubility in the iron phase. Combined with the phosphorus partitioning model between the lunar mantle and core, we further constrained the phosphorus content in the lunar core.

2. METHODS

Stoichiometric amounts of red phosphorus (99.9 wt%, Alfa Aesar) and iron powder (99.99 wt%, Alfa Aesar) were mechanically mixed and ground under ethanol in an agate mortar to synthesize FeP by solid-state reaction. After air-drying of the mixture, it was pre-compressed and loaded into a 6 mm length hexagonal boron nitride capsule (h-BN, ϕ 4 mm) and then sealed and stored in a desiccator. FeP was synthesized at 1 GPa and 1000 °C for 3 hours in a multi-anvil apparatus. These *P-T* conditions are the same as those used by Gu et al. (2011). The recovered sample was identified by powder X-ray diffraction to be a pure FeP phase. We then use FeP and pure iron powder as the starting materials. Synthesized FeP is used in this study because it is representative of proto-phosphorus and widely distributed in meteorites. A similar starting material was also used in the Fe-FeS studies by Fei et al. (1997, 2000).

All experiments were conducted on a DS 6×600 t cubic-anvil-type apparatus with WC anvils of 23.5 mm truncation edge length at the Institute of Geochemistry, Chinese Academy of Sciences, Guiyang, China. The synthesized FeP powder was thoroughly mixed with a pure iron powder to prepare different starting materials with phosphorus contents varying from 5.8 to 27 wt%. Three different starting materials were put into a boron nitride capsule, as shown in Fig. 2. An Al_2O_3 sleeve thermal insulator and a graphite heater were used in the sample assembly. The pressure was calibrated by the quartz phase transition and NaCl melting curve at high pressures and high temperatures (Bose and Ganguly, 1995; Rybacki et al., 1998). The uncertainty for the pressure is ±0.2 GPa. Temperatures were monitored by a W5%Re-W26%Re thermocouple which was placed close to the sample, with the uncertainty of ±5 °C. The temperature gradient from the sample center to the thermocouple was less than 10 °C, measured by two thermocouples in another experiment. All the runs were carried out from 1075 to 1600 °C with an interval of 50 or 100 °C. Samples were compressed up to 3 GPa and heated to the designed temperature with a heating rate of 60 °C/min, and then held at that temperature for 8 or 10 hours for each experiment. The runtime was chosen by different starting component and referred to the equilibrium time in the experiments by Stewart and Schmidt (2007). Run products were then quenched by shutting down the power. Several products (run# FP-1-1, FP-7-1) were ground into powders for X-ray diffraction analyses, and the others were mounted in epoxy, polished carefully and carbon-coated for quench texture and chemical composition analyses.

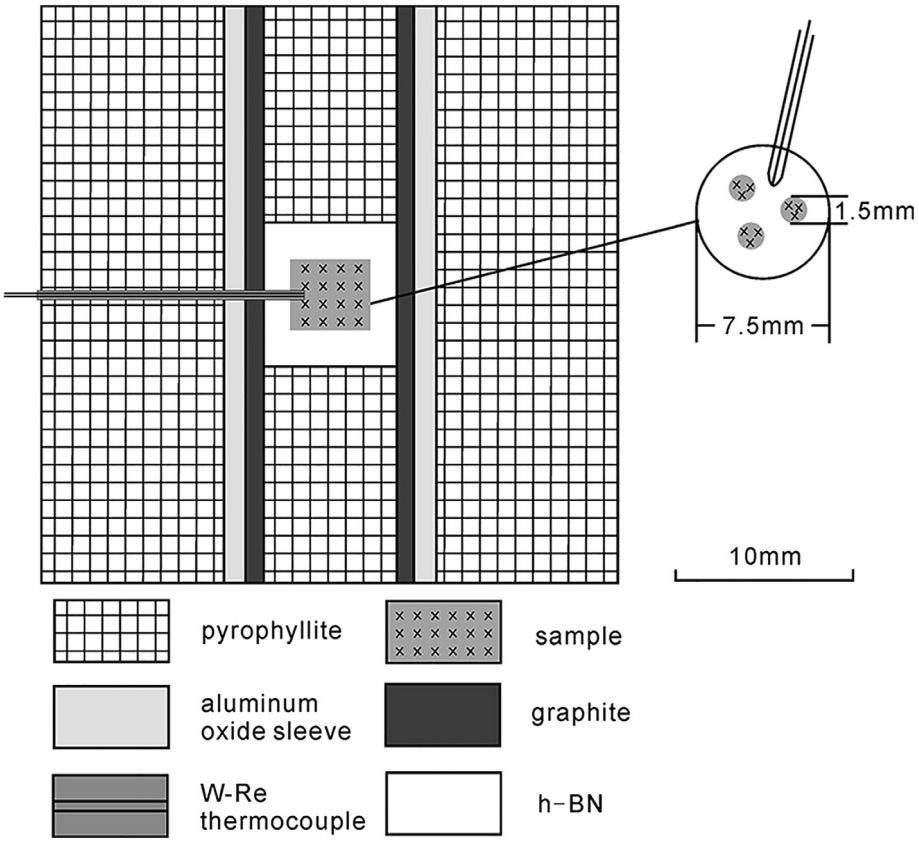

Fig. 2. Cross section of the sample assemblage used in this study.

Powder X-ray diffraction patterns of several quenched samples were collected using an X-ray diffractometer with Cu-Kα radiation. The iron phosphide phases (FeP, Fe_2P, and Fe_3P) had lattice parameters consistent with previous results (Table 1). We also checked the quenched iron sample from the run of FP-7-2 ($Fe_{94.2}P_{5.8}$) by micro-focused X-ray diffraction analyses, using a RIGAKU D/Max Rapid IIR micro-diffractometer operated at 40 kV and 250 mA. The X-ray wavelength of Cu-Kα1 generated from copper anode and graphite monochromatic is 1.54056 Å. The two-dimensional diffraction data were converted to one-dimensional (2θ-I) data by Display software of the instrument. The result is shown in Fig. 3.

The chemical composition analyses were performed by using a JXA-8230 electron microprobe operated at 20 kV and 10 nA at the Testing Center of Shandong Bureau, China. Iron and phosphorus were analyzed by wavelength dispersive spectrometry (WDS) employing analytical standards of pure iron and apatite, respectively. The ratios of peak/background for phosphorus in the low-P iron are generally ~11 at our experimental conditions. Nitrogen, boron, and oxygen were also directly analyzed as potential contaminants, using GaN, B metal, and Al_2O_3 as standards. There are no significant signals during analyses with the peak and background counting times of 20 s and 10 s respectively. Heterogeneity in the quenched melt phase is common in quenched metal alloys. To ensure representative compositions, a fully focused beam was used for crystalline iron and iron phosphide and beam diameter of 20–50 μm was used for quenched melt domains. It is as the same as the method used by Stewart and Schmidt (2007) and Dasgupta et al. (2009). Usually, 10 to 15 points were analyzed for the melts and solid phases. Final results were reduced by a ZAF correction method (Armstrong, 1995) and are listed in Table 2.

3. RESULTS AND DISCUSSIONS

3.1. Fe-P phase diagram and previous studies

Backscattered electron images of the run products show unambiguous quench textures of the molten samples (Fig. 4). Below the melting temperatures, different mineral phases are present in solid xenomorphic-granular phases and have obvious grain boundaries. Quenched liquids have the similar dendritic growth textures as described by Stewart and Schmidt (2007) in the Fe-P-S system at 23 GPa and by Dasgupta and Walker (2008) in the Fe-C system at 2 GPa. In the phosphorus-rich runs, some samples undergo partial melting with small mineral chips scattered in the melts (Fig. 4g). The temperature of the Fe-P eutectic on the iron-rich side is constrained at ~1085 °C due to the Fe-P liquid which appears from 1075 to 1100 °C (Fig. 4a–f). The mixture of FeP and Fe_2P begins to melt at about 1400 °C (Fig. 4h, i). In the run of $Fe_{81.8}P_{18.2}$, crystalline $Fe_2P + Fe_3P$ disappears and quenched Fe-P melt coexists with crystalline Fe_2P when T > 1185 °C.

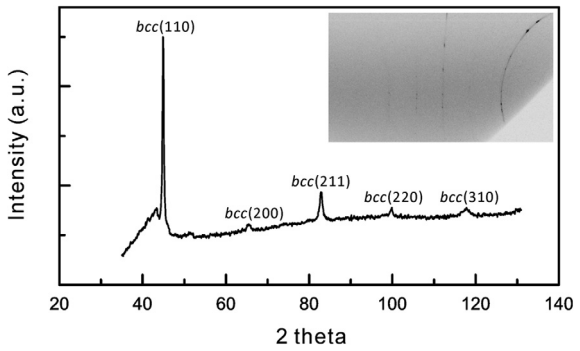

Fig. 3. Micro-focused X-ray diffraction analyses to the run product of FP-7-2 ($Fe_{94.2}P_{5.8}$). X-ray beam size with diameter of 200 μm was used to analyze the interest region. The inset shows a two-dimensional diffraction pattern which was collected by the detector. The background of the diffraction data remains. Only the peaks of body-center cubic structure of iron are found and labeled with corresponding crystal indices (hkl).

With increasing temperature, the phosphorus content in the liquid Fe-P decreases from ~10.1 wt% at 1100 °C to ~9.0 wt% at 1500 °C. The solubility of phosphorus in the solid iron is 0.7–1.3 wt% depending on the temperatures (Table 2). Some crystalline solid iron phases containing ~2.8 wt% phosphorus are noted in the run below 1250 °C and coexist with low-P solid iron (Table 2). The runs on the iron-rich side at 2 GPa indicate that 0.7–1.0 wt% phosphorus could dissolve in the solid iron (Table 2). Compared with ideal iron phosphides, the experimental products of FeP, Fe_2P, and Fe_3P have a slight excess of iron and this phenomenon also occurs in the Fe-P system at 23 GPa (Stewart and Schmidt, 2007).

3.2. Pressure effects on the Fe-P eutectic

The Fe-P phase diagram at 3 GPa (Fig. 5a) is widely consistent with the topology of phase diagram at ambient pressure (Zaitsev et al., 1995) and 23 GPa (Stewart and

Table 1
Lattice parameters of iron phosphide phases produced in this study and previous works.

	Space group	a	b	c	V(Å^3)	Ref.
FeP	*Pnma*	5.1862(3)	3.0965(2)	5.7868(3)	92.93(1)	This study
		5.1826(6)	3.0976(3)	5.7838(7)	92.85(1)	Gu et al. (2011)
Fe_2P	*P-62m*	5.8651(1)		3.4555(1)	102.94(1)	This study
		5.8764(3)		3.4493(1)	103.14	Dera et al. (2008)
		5.8650(10)		3.456(1)	102.95(3)	Scott et al. (2008)
Fe_3P	*I-4*	9.0998(2)		4.4615(2)	369.44(2)	This study
		9.099(2)		4.463(2)	369.5(2)	Scott et al. (2007)
		9.1003(1)		4.4685(1)	370.06(1)	Gu et al. (2014)

Table 2
Starting materials, experimental conditions, coexisting phases, and phase compositions in the run products of Fe-P system at 2 and 3 GPa.

Run #	t, h	T, °C	Starting materials (wt %)	Phases	P	Fe	Total
P = 3 GPa							
FP-7-1	8	1075	$Fe_{94.2}P_{5.8}$	Fe_3P	15.16(7)[a]	85.50(49)	100.65(55)
				α-Fe	2.95(3)	98.40(25)	101.35(23)
					1.40(1)	98.46(27)	99.86(25)
			$Fe_{90}P_{10}$	Fe_3P	15.17(4)	85.46(27)	100.85(24)
				α-Fe	2.92(2)	97.37(11)	100.28(9)
					1.32(5)	99.48(22)	100.80(20)
			$Fe_{86.3}P_{13.7}$	Fe_3P	15.22(9)	85.13(36)	100.34(36)
				α-Fe	1.13(1)	98.37(29)	99.50(29)
FP-7-2	8	1100	$Fe_{94.2}P_{5.8}$	Melt	10.10(33)	90.11(52)	100.21(27)
				α-Fe	2.94(3)	97.62(56)	100.56(58)
					1.35(1)	98.84(42)	100.19(41)
			$Fe_{90}P_{10}$	Melt	10.39(47)	90.34(51)	100.74(37)
				α-Fe	3.05(2)	97.21(29)	100.26(29)
			$Fe_{86.3}P_{13.7}$	Fe_3P	15.21(3)	85.52(10)	100.73(10)
				Melt	8.83(26)	91.58(32)	100.41(23)
FP-1-1	10	1150	$Fe_{94.2}P_{5.8}$	Melt	9.98(30)	88.78(57)	98.75(50)
				α-Fe	1.32(2)	98.33(38)	99.65(40)
			$Fe_{81.8}P_{18.2}$	Fe_3P	14.91(3)	84.94(19)	99.85(18)
				Fe_2P	21.05(8)	79.42(20)	100.48(20)
			$Fe_{73}P_{27}$	Fe_2P	21.04(8)	78.44(26)	100.38(33)
				FeP	34.40(21)	65.31(32)	98.42(50)
FP-7-3	8	1185	$Fe_{94.2}P_{5.8}$	Melt	10.62(23)	88.24(29)	100.84(20)
				α-Fe	1.32(5)	98.77(27)	100.09(28)
			$Fe_{90}P_{10}$	Melt	10.26(35)	90.17(14)	100.44(23)
				α-Fe	2.40(32)	97.93(44)	100.33(22)
			$Fe_{81.8}P_{18.2}$	Melt	10.93(23)	88.81(33)	99.74(34)
				Fe_2P	21.13(13)	79.49(41)	100.61(46)
FP-1-2	10	1200	$Fe_{94.2}P_{5.8}$	Melt	9.78(36)	89.45(81)	99.24(72)
				α-Fe	1.26(2)	99.02(48)	100.28(51)
			$Fe_{81.8}P_{18.2}$	Melt	9.60(54)	89.35(87)	98.94(43)
				Fe_2P	20.96(9)	79.63(18)	100.59(20)
			$Fe_{73}P_{27}$	Fe_2P	20.97(6)	79.59(35)	100.56(40)
				FeP	34.78(13)	65.9(13)	100.68(24)
FP-1-3	8	1225	$Fe_{81.8}P_{18.2}$	Melt	9.62(34)	89.31(36)	98.92(42)
				Fe_2P	20.72(9)	79.13(24)	99.85(28)
			$Fe_{73}P_{27}$	Fe_2P	20.84(7)	78.71(50)	99.55(53)
				FeP	34.30(17)	65.44(49)	99.74(61)
FP-2-1	8	1250	$Fe_{94.2}P_{5.8}$	Melt	9.67(16)	89.38(40)	99.05(53)
				α-Fe	1.24(1)	97.92(11)	99.16(11)
			$Fe_{90}P_{10}$	Melt	10.03(38)	90.31(43)	100.34(16)
				α-Fe	2.91(21)	96.76(29)	99.67(18)
			$Fe_{86.3}P_{13.7}$	Melt	9.46(25)	89.84(37)	99.29(45)
				Fe_3P	15.22(10)	85.37(26)	100.59(36)
FP-2-3	10	1325	$Fe_{94.2}P_{5.8}$	Melt	9.88(24)	90.73(14)	100.61(18)
				α-Fe	1.06(1)	99.13(17)	100.19(18)
			$Fe_{81.8}P_{18.2}$	Melt	11.08(47)	89.37(37)	100.44(17)
				Fe_2P	21.14(8)	79.59(41)	100.72(46)
			$Fe_{73}P_{27}$	Melt	25.93(40)	74.91(57)	100.83(44)
				Fe_2P	21.18(5)	79.56(10)	100.75(7)
				FeP	34.4(35)	66.28(52)	100.68(48)
FP-3-1	8	1350	$Fe_{94.2}P_{5.8}$	Melt	9.53(14)	91.04(29)	100.57(19)
				α-Fe	1.14(2)	98.71(40)	99.84(39)
			$Fe_{90}P_{10}$	Melt	9.52(27)	90.21(29)	99.73(20)
			$Fe_{86.3}P_{13.7}$	Melt	12.87(38)	87.09(36)	99.97(26)
FP-3-2	8	1375	$Fe_{94.2}P_{5.8}$	Melt	10.36(46)	89.87(73)	100.22(36)
				α-Fe	1.31(2)	98.25(33)	99.57(32)
			$Fe_{81.8}P_{18.2}$	Melt	10.37(19)	89.86(31)	100.23(15)
				Fe_2P	21.19(10)	79.88(39)	101.08(44)
			$Fe_{73}P_{27}$	melt	26.28(34)	74.28(41)	100.56(40)
				Fe_2P	21.08(18)	79.17(17)	100.24(32)
				FeP	34.62(8)	65.66(33)	100.28(39)

(*continued on next page*)

Table 2 (*continued*)

Run #	t, h	T, °C	Starting materials (wt %)	Phases	P	Fe	Total
FP-3-3	10	1400	$Fe_{94.2}P_{5.8}$	Melt	9.42(15)	91.01(26)	100.43(22)
				α-Fe	1.05(1)	100.12(37)	101.17(37)
			$Fe_{90}P_{10}$	Melt	9.77(7)	91.04(18)	100.81(16)
			$Fe_{86.3}P_{13.7}$	Melt	13.58(21)	87.21(33)	100.79(23)
				Melt	9.39(18)	90.85(22)	100.24(3)
FP-4-1	10	1425	$Fe_{94.2}P_{5.8}$	Melt	9.13(17)	91.25(28)	100.25(26)
				α-Fe	0.96(2)	99.42(35)	100.38(34)
			$Fe_{81.8}P_{18.2}$	Melt	13.26(126)	86.50(91)	99.75(36)
				Fe_2P	20.91(6)	80.32(27)	101.23(31)
FP-4-3	8	1475	$Fe_{94.2}P_{5.8}$	Melt	8.60(22)	91.18(35)	99.78(33)
				α-Fe	0.71(00)	100.27(20)	100.97(19)
			$Fe_{81.8}P_{18.2}$	Melt	14.65(57)	84.97(57)	99.63(22)
				Fe_2P	20.91(14)	79.60(21)	100.51(32)
			$Fe_{73}P_{27}$	Melt	26.33(40)	73.31(48)	99.65(20)
				Fe_2P	21.27(15)	79.27(18)	100.54(9)
				FeP	34.45(40)	66.25(35)	100.70(31)
FP-5-1	8	1500	$Fe_{94.2}P_{5.8}$	Melt	8.20(17)	90.45(23)	98.65(22)
				α-Fe	0.78(3)	98.96(24)	99.74(25)
FP-5-3	8	1550	$Fe_{94.2}P_{5.8}$	Melt	10.02(26)	89.71(27)	99.73(12)
				α-Fe	1.01 (2)	98.75(13)	99.76(13)
FP-6-1	8	1600	$Fe_{94.2}P_{5.8}$	Melt	9.61(13)	89.61(15)	99.22(13)
				α-Fe	0.73(2)	98.58(17)	99.31(15)
P = 2 GPa							
FP-9-1	10	1200	$Fe_{94.2}P_{5.8}$	Melt	11.14(37)	89.67(31)	100.81(23)
				α-Fe	1.07(3)	99.74(38)	100.80(36)
FP-9-2	6	1350	$Fe_{94.2}P_{5.8}$	Melt	9.80(42)	89.40(26)	99.20(25)
				α-Fe	0.81(2)	98.71(34)	99.52(34)
FP-9-3	6	1500	$Fe_{94.2}P_{5.8}$	Melt	9.52(28)	90.93(40)	100.45(33)
				α-Fe	0.82(5)	98.77(25)	99.59(28)

[a] Values in wt%. Numbers in parentheses indicate standard error of the mean based on replicate analyses ($\delta_M = \delta/\sqrt{n}$).

Schmidt, 2007). Liquidus temperatures on the iron-rich side ($Fe_{94.2}P_{5.8}$) is 1375–1400 °C which is about 100 °C higher than the temperatures determined by in-situ ultrasonics at 1257 ± 50 °C and 4 GPa with starting P content of 5 wt% (Chantel et al., 2018). The reason is possibly the large uncertainty (±50 °C) in their measured experimental temperatures. The eutectic temperature on the iron-rich side is 1085 °C, about 40 °C higher than the 1048 °C eutectic at ambient pressure and 190 °C lower than the 1275 °C eutectic at 23 GPa (Stewart and Schmidt, 2007). Among the Fe-C, Fe-P and Fe-S systems, Fe + Fe_3S has the lowest eutectic temperature of 1100 °C under the similar pressure (~21 GPa, Fei et al., 2000). Around 3 to 5 GPa, the Fe-P eutectic temperature on the iron-rich side is ~100 °C lower than that of the Fe-C system (Hirayama et al., 1993; Fei and Brosh, 2014) and ~100 °C higher than the Fe-S system (Usselman, 1975). Phosphorus shows a moderate contribution to reducing the melting temperature of the iron alloy, which is significant for the formation of a liquid outer core in the Earth and terrestrial planets.

The eutectic liquid contains ~10.5 wt% P at ambient pressure and ~9 wt% P at 23 GPa, which suggests the solubility of phosphorus in the Fe-P eutectic liquid decreases with increasing pressures (Fig. 1). There is about 10.1 wt % P dissolved in the eutectic liquid at 3 GPa. In contrast, pressure has a positive effect on the maximum phosphorus solubility in the solid iron. As much as 4 wt% P is detected in the crystalline solid iron at 23 GPa, more than the result of 2.6 wt% P at ambient pressure (Fig. 1a and b). The crystalline solid iron phase contains up to 2.9 wt% P at 3 GPa in the present study, slightly higher than the value at ambient pressure.

3.3. Low-P and high-P crystalline solid iron

There are two iron phases on the iron-rich side, α-Fe (body-center-cubic, *bcc* structure) and γ-Fe (face-center-cubic, *fcc* structure) in the Fe-P phase diagram at ambient pressure (Fig. 1a). With increasing phosphorus content in the iron, the α-Fe is more stable because the P is a *bcc*-stabilizer and is thought to narrow down the stable temperature range of the γ-phase iron by forming the so-called "γ-loop" (Pepperhoff and Acet, 2001).

We analyzed the iron phase in a region which is as the same area of Fig. 4f (element mapping was shown in Fig. 6a). The structure of the quenched iron is the body-center cubic (*bcc*-Fe) (Fig. 3). Therefore, the two different P-bearing solid irons are both α-Fe which stable region is consistent with previous studies (Okamoto, 1990; Perrot et al., 2002). According to the Fe-P phase diagram at ambient pressure (Fig. 1a), there must be a 2-phase loop between the α-Fe and γ-Fe, called α + γ region that was shown in Fig. 5(b). The γ-Fe is generally considered to be unquenchable (Pepperhoff and Acet, 2001). Stability of γ-iron in the

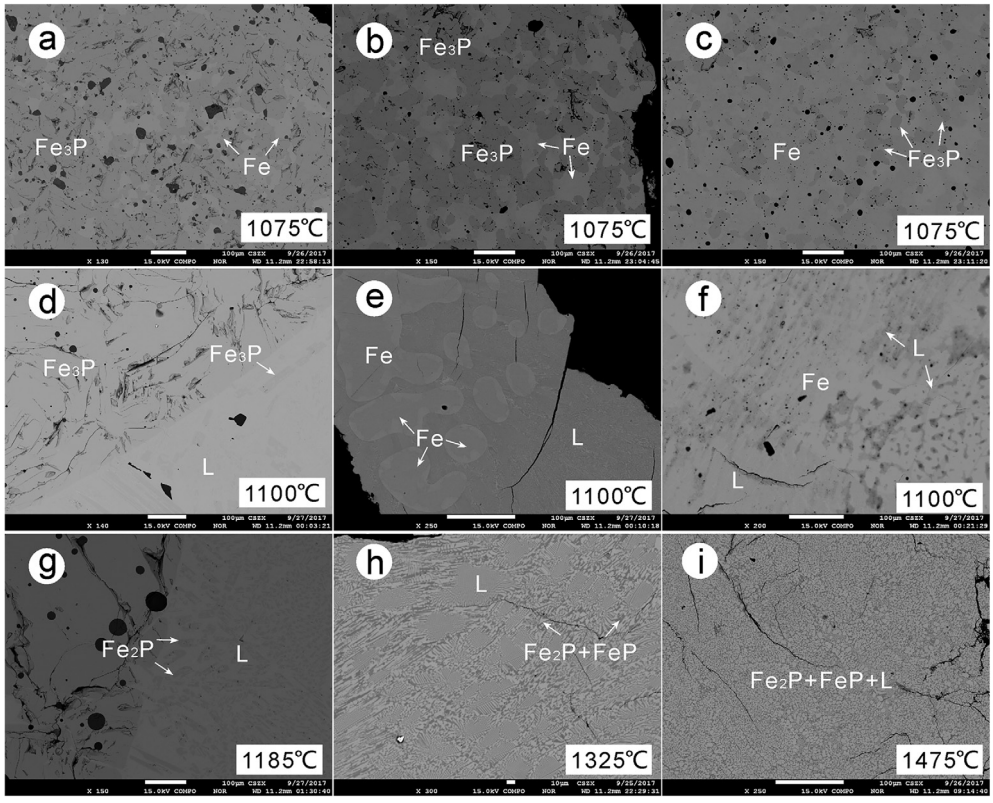

Fig. 4. Backscattered electron images of the run products of FP-7-1 (a, b, c), FP-7-2 (d, e, f), FP-7-3 (g), FP-2-3 (h) and FP-4-3 (i). Images of a (d), b(e) and c(f) indicate the quenched phase structure of $Fe_{86.3}P_{13.7}$, $Fe_{90}P_{10}$ and $Fe_{94.2}P_{5.8}$ respectively. The black phases disseminated in Fe and Fe_3P are holes created during polishing because Fe-P alloy is fragile.

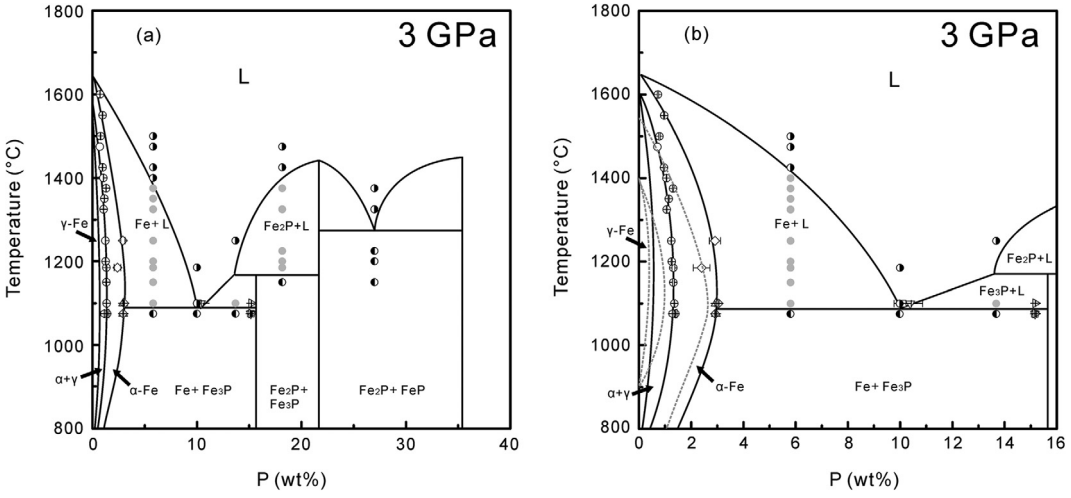

Fig. 5. (a) is the phase diagram of Fe-P system at 3 GPa given by this study. (b) is a close-up phase diagram on the iron-rich side (0–16 wt% P). Pure iron melting temperature is taken from Liu and Bassett (1975). The phase stable range of γ-Fe is referred from the iron phase diagram by Acet et al. (2001). Righ-black, grey, and left-black circles represent liquid, solid + liquid, and solid minerals, respectively, in run products of different starting materials and different temperatures. Open symbols with error bars are P concentration in the iron, melts, and iron phosphide. Solidus and liquidus are determined by partial-melting temperatures and full-melting temperatures. The dashed lines in (b) are solidus curves for γ-Fe, γ+α iron, and α-Fe at ambient pressure reported by Okamoto (1990).

metallic meteorites also strongly depends on the chemical composition and cooling-rate (Uhlig, 1954). The solubility of P in γ-Fe has been measured by various indirect methods, such as thermal analysis, metallography and magnetic measurement (Haughton, 1927; Vogel, 1929; Roquet and Jegaden, 1951; Lorenz and Fabritius, 1962; Fisher et al.,

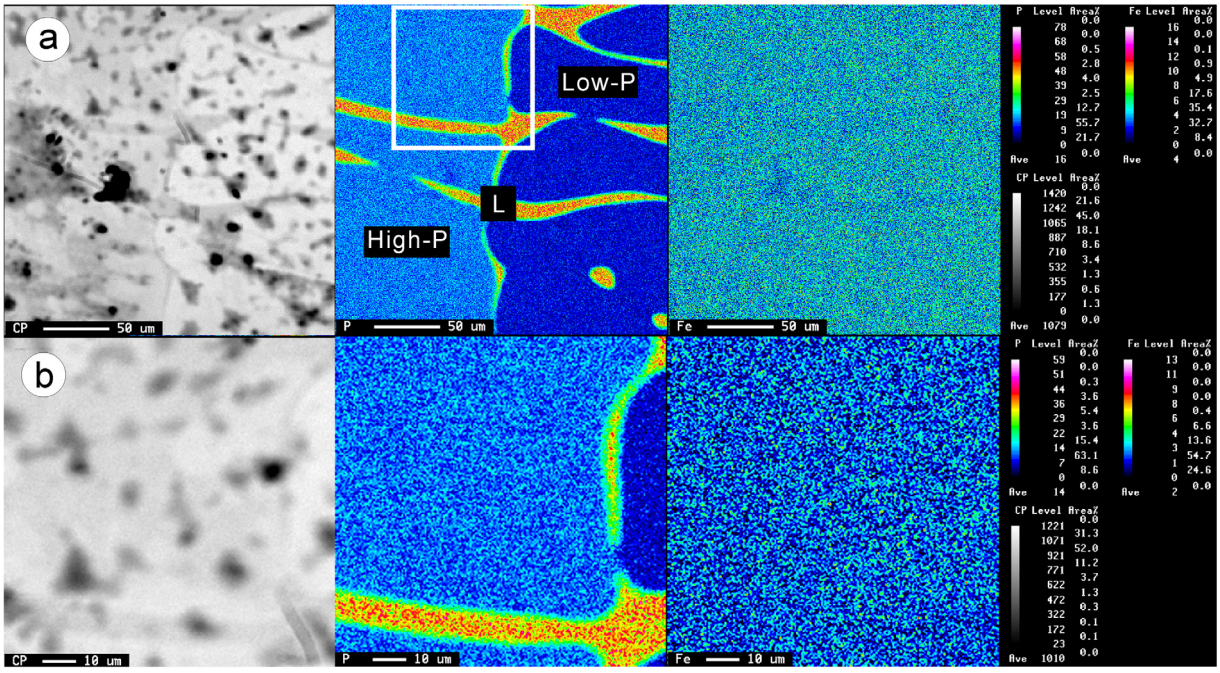

Fig. 6. Selected EPMA mapping analyses of the quenched sample of $Fe_{94.2}P_{5.8}$ at 1100 °C at 3 GPa. Image (b) is a close-up of the white square region in the image (a). Pictures shown from left to right are backscattered electron image, P-mapping image and Fe-mapping image, respectively. Low-P and High-P represent low P and high P concentration iron.

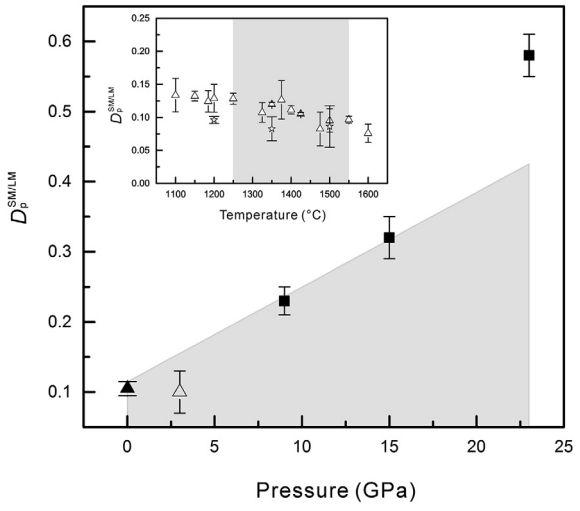

Fig. 7. Partition coefficient of phosphorus between solid metal and liquid metal varies with pressures ($T = 1250$–1550 °C). The inset is the measured $D_p^{SM/LM}$ in Fe-P binary system from this study at the temperatures from 1100 to 1600 °C. Open triangles and stars are the results at 3 and 2 GPa, respectively. Solid squares are the $D_p^{SM/LM}$ in Fe-Ni-S-P system from Stewart et al. (2009) with S content of 8–14 wt%. Solid triangle is the data calculated from S-free to 8 wt% S in the liquid metal for Fe-S-P system at ambient pressure (Righter and Drack, 2000). There is a linear trend for $D_p^{SM/LM}$as increasing pressures in Fe-S-P system. Grey area in the inset figure is the potential temperatures at the current lunar core-mantle boundary. Trapezoid grey area is the possible $D_p^{SM/LM}$ at various pressure and sulfur content situations.

1966). Thermodynamic calculations predict that the maximum solubility of phosphorus in solid γ-Fe is ~0.3 wt% at ~1150 °C and ambient pressure (Lorenz and Fabritius, 1962; Okamoto, 1990). On the other hand, according to the extrapolation from Fe-P-C and Fe-P-Ni experiments, the metastable solubility of P in γ-Fe at ambient pressure is estimated at 1.1, 0.6, 0.3 wt% at 1000, 900, 800 °C, respectively (Kaneko et al., 1965).

3.4. Phosphorus partition coefficient between the solid metal and liquid metal

Using the phosphorus concentration in the iron and melts with starting materials of $Fe_{94.8}P_{5.2}$, we calculate the phosphorus partition coefficient between the solid and liquid metal ($D_p^{SM/LM}$). The value of the $D_p^{SM/LM}$ decreases with increasing temperature (Fig. 7). At the modeled temperatures for the lunar core-mantle boundary, 1200–1550 °C, the $D_p^{SM/LM}$ is 0.10 ± 0.03 at 3 GPa. It is consistent with the partition coefficient formula at ambient pressure given by Righter and Drake (2000). They indicate that the natural logarithm of $D_p^{SM/LM}$ has a linear relationship with the sulfur content in the melts: $\ln D_p^{SM/LM} = 16.19 \times (Xs)^2 - 2.42$, where Xs is sulfur mole fraction. Thus, the $D_p^{SM/LM}$ are 0.095 with sulfur-free and 0.115 with 8 wt% ($Xs = 0.13$). It is obvious that more phosphorus is into solid iron with the addition of S. For pressures, the $D_p^{SM/LM}$ at 3 GPa is slightly higher than the result at 2 GPa which suggests that more phosphorus would be dissolved in the solid iron at

high pressures. In the study of Fe-S-P system at high pressures, $D_{\mathrm{p}}^{\mathrm{SM/LM}}$ increase from 0.23 ± 0.02 at 9 GPa, 0.32 ± 0.03 at 15 GPa to 0.58 ± 0.03 at 23 GPa (Stewart et al., 2009). The result at 23 GPa is beyond the trend because the sulfur content is 13 ± 1 wt%, higher than the lower pressure experiments (8–10 wt%).

4. PHOSPHORUS IN THE LUNAR CORE

4.1. Phosphorus budget in the lunar core by partitioning model

The Moon has a small metallic core that has been supported by numerous geochemical and geophysical studies (Kuskov and Kronrod, 1998; Righter, 2002; Weber et al., 2011; Williams et al., 2014). There are three factors controlling the phosphorus content in the lunar core ($C_{\mathrm{core}}^{\mathrm{P}}$): phosphorus partition coefficient between the core and mantle ($D_{\mathrm{P\text{-}Moon}}^{\mathrm{core/mantle}}$), core mass, and the phosphorus content in the initial bulk Moon ($C_{\mathrm{BM}}^{\mathrm{P}}$). Through a simple model of mass differentiation (core's mass is set at 2.5 wt% of the bulk Moon), the $C_{\mathrm{core}}^{\mathrm{P}}$ could be calculated by the following equation:

$$C_{\mathrm{core}}^{\mathrm{P}} = \frac{C_{\mathrm{BM}}^{\mathrm{P}}}{1/D_{\mathrm{P\text{-}Moon}}^{\mathrm{core/mantle}} + 0.025(1 - 1/D_{\mathrm{P\text{-}Moon}}^{\mathrm{core/mantle}})} \quad (1)$$

On the one hand, according to the cosmochemical composition models suggested by Allègre et al. (1995) and McDonough (2003), the *D*core/mantle P-Earth of the Earth is calculated as 20–50, which has large uncertainty because of volatile-loss (Halliday and Wood, 2010; Righter, 2011).

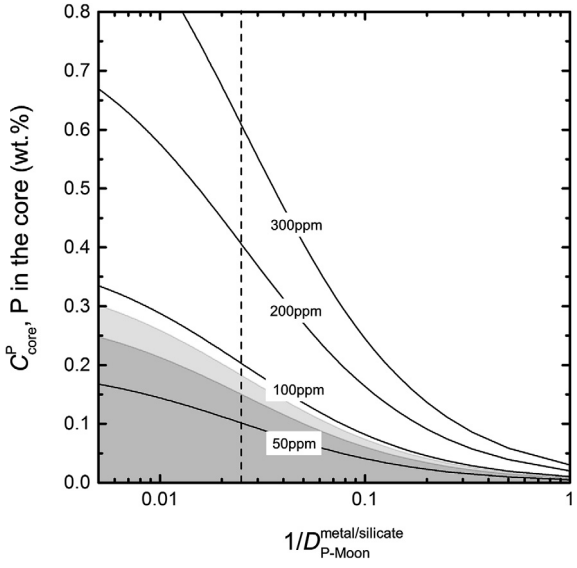

Fig. 8. Phosphorus concentration in the lunare core, $C_{\mathrm{core}}^{\mathrm{P}}$ as a function of P storage in the initial Moon and reciprocal of partition coefficient of phosphorus between core and mantle, $1/D_{\mathrm{P\text{-}Moon}}^{\mathrm{core/mantle}}$. The initial bulk Moon phosphorus content ($C_{\mathrm{BM}}^{\mathrm{P}}$) are plotted as curves varying from 50 to 300 ppm. Verticle dashed line is the lowest estimate of $D_{\mathrm{P\text{-}Moon}}^{\mathrm{core/mantle}}$ at 40. Light grey area is the result of P core storage with a BSE-like P content (82 ± 8 ppm) in the initial bulk Moon.

The Moon has a similar partition coefficient (39–69) to the Earth (Steenstra et al., 2016a). But, this value should be reexamined because it is based on the relatively low $C_{\mathrm{BM}}^{\mathrm{P}}$ (43 ppm) suggested by O'Neill (1991) and Righter (2002). Their estimate for the $C_{\mathrm{BM}}^{\mathrm{P}}$ is significantly influenced by the siderophile elements abundance of the impactor. On the other hand, the partition experiments for the phosphorus between the metal and silicate melt provide more constrains. Steenstra et al. (2015) extended the phosphorus partition coefficient formula by combining all available experimental metal-silicate partitioning data from a wide range of studies conducted at core conditions of the Moon. The formula proposed a modeled log $D_{\mathrm{P\text{-}Moon}}^{\mathrm{core/mantle}}$ between 1.9 and 2.3 ($D_{\mathrm{P\text{-}Moon}}^{\mathrm{core/mantle}} = 79$–$200$) corresponding to the metal-silicate equilibration of a sulfur-rich (11 wt% in the core) and nickel-bearing metallic core at the conditions of $P \approx 4$ GPa, $T = 2377$ °C, $\Delta\mathrm{IW} = -2.15$. However, there may be a lower temperature condition for the lunar magma ocean (LMO): $T = 1900$ °C, $\Delta\mathrm{IW} = -2.2$, $X_{\mathrm{S}} = X_{\mathrm{C}} = 0$, where X_{S} and X_{C} are mole fraction of S and C in the melts (Righter, 2002, 2003; Righter et al., 2009; Rai and Van Westrenen, 2014). The high S content in the lunar core would result in lower modeled core formation temperatures and vice versa (Rai and van Westrenen, 2014; Steenstra et al., 2016a). The phosphorus partition coefficient will decrease with decreasing temperatures (Righter et al., 2010). It is also possible for an intermediate LMO. The metal-silicate equilibration in the Moon could also happen at the pressure of 3 GPa (Elkins-Tanton et al., 2011), corresponding to the pressure of a lunar magma ocean with a depth of ~650 km where deep moonquakes occur (>700 km, Nakamura et al. 1973). When we take the cosmochemical models and partition coefficient experimental models into account, the $D_{\mathrm{P\text{-}Moon}}^{\mathrm{core/mantle}}$ in this study is set at a range from 40 to 200. According to the Eq. (1), we plot the $C_{\mathrm{core}}^{\mathrm{P}}$ against the $C_{\mathrm{BM}}^{\mathrm{P}}$ ranging from 50 to 300 ppm and different $D_{\mathrm{P\text{-}Moon}}^{\mathrm{core/mantle}}$ (40–200), as shown in the Fig. 8.

Previous estimates of $C_{\mathrm{BSM}}^{\mathrm{P}}$ and $C_{\mathrm{BM}}^{\mathrm{P}}$ was 20 ppm and 43 ppm, respectively, which resulted in ~0.1 wt% P content in the lunar core (O'Neill, 1991). However, the phosphorus content in the bulk Moon ($C_{\mathrm{BM}}^{\mathrm{P}}$) is probably underestimated. More evidence from the elemental and isotopic studies indicates that the composition of the bulk Moon is more similar to the bulk silicate Earth (BSE) (Zhang et al., 2012; Dauphas et al., 2014; Taylor and Wieczorek, 2014). Therefore, using a BSE-like phosphorus concentration (82 ± 8 ppm, Wang et al., 2018) as the $C_{\mathrm{BM}}^{\mathrm{P}}$ may be more appropriate for the initial silicate Moon. Such value would result in a slightly higher P content ($C_{\mathrm{core}}^{\mathrm{P}}$, 0.1–0.3 wt%) in the lunar core (Fig. 8). Moreover, the bulk silicate Moon enriched in crustal components model (the cBSM model) suggest that up to 0.04 wt% P_2O_5, equal to 174 ppm P, was present in the initial silicate Moon after the giant impact (Togashi et al., 2017). It would form a P-bearing core with 0.35–0.58 wt% phosphorus in the most optimistic scenario.

Here we used a moderate core mass (2.5 wt%) in the model to be consistent with previous studies (Kuskov and

Kronrod, 1998 2.5 ± 2 wt%; Steenstra et al., 2016a 2.5 ± 0.1 wt%). The smaller lunar core with ≤ 1.5 wt% mass was also suggested by Williams et al. (2014) according to the geophysical measurements obtained by GRAIL. Lowering the core mass will lead to higher phosphorus concentration in the lunar core (Eq. (1)). In this case, the P core storage would be 0.45 wt% (core mass = 1.5 wt% of bulk Moon mass, $C^{P}_{BM} = 90$ ppm, and $D^{core/mantle}_{P\text{-}Moon} = 200$), larger than 0.30 wt% P with a 2.5 wt% core.

4.2. Phosphorus in a Fe-Ni-S-C lunar core

The thermal state of the lunar core has been discussed and described in different models depending on the geophysical and geochemical data. For the current temperature at the core-mantle boundary, there is a wide range from ~1200 °C (Chacko and De Bremaecker, 1982; Ziethe et al., 2009; Scheinberg et al., 2015) to 1377 °C (Spohn et al., 2001), to as high as ~1500 °C (Zhang et al., 2013; Laneuville et al., 2014; Scheinberg et al., 2015). Pressure at the core-mantle boundary and inner core are speculated as 4.5 and 5.3 GPa, respectively (Kuskov and Kronrod, 1998; Garcia et al., 2011). To crystallize a solid iron core in the Moon, the upper limit to the core's temperature should be ~1700 °C at 5.3 GPa, according to the iron phase diagram (Pepperhoff and Acet, 2001). As shown in the Fig. 5, the phosphorus solubility in the iron crystalline is ~0.7 wt% at 1500 °C and 3 GPa. At higher temperatures, $T = 1600$ °C, its solubility is slightly higher. Combined with the multiple effects from the temperatures and pressures on the phosphorus solubility in the iron, the maximum P content dissolved in the iron is assessed as 0.85 ± 0.15 wt% at the lunar core conditions (4.5–5.3 GPa and 1500 ~1700 °C).

The lunar core is assumed to have a complex chemical composition system such as Fe-Ni-S-C (Righter et al., 2017). Nickel is considered a major alloying element in the lunar core and has a wide concentration ranging from 9 to 30 wt% (Righter, 2002; Righter et al., 2017). In a scenario where the LMO equilibrated with the lunar core at pressures > 3 GPa, the Ni core storage will be 10–24 wt% (Steenstra et al., 2017). Carbon in the lunar core is reassessed to be ~1.2 wt% by Righter et al. (2017) but no more than 2.0 wt% according to the Fe-C phase diagram at 5 GPa (Fei and Brosh, 2014). Lunar core is also expected to have a higher C content range of ~0.6–4.8 wt%, given high C abundance in the BSM (Steenstra et al., 2017) which is also consistent with the high amount of C in the lunar mantle (Wetzel et al., 2015). As for bulk S content in the lunar core, there is still in debate whether the core is sulfur-rich (Weber et al., 2011 < 6 wt%) or sulfur-poor (Steenstra et al., 2017 < 0.16 wt%).

Experiments on the Fe-Ni-P system at ambient pressure suggest that nickel has a weak influence on the phosphorus solubility in γ-Fe (12 wt% Ni). Approximately 0.1 wt% P was reduced in γ-Fe-Ni at 1000, 900 and 800 °C (Kaneko et al., 1965). It is similar to the decrease of C content in the Fe-Ni-C melt at ambient pressure (Tsymbulov and Tsmekhman, 2001) and 2 GPa (Dasgupta and Walker, 2008). About 1 wt% carbon in the solid Fe-Ni(12 wt%)-P alloy could reduce 50% phosphorus concentration at 800–1000 °C by experiments (Kaneko et al., 1965). The C-bearing partitioning experiment shows that ~76% phosphorus is reduced in the liquid Fe-C metal at 5 GPa and 2000 °C (Jana and Walker, 1997). Sulfur in the iron-light element system may depress P concentration, similar to the sulfur depression on carbon in the Fe-Ni-S-C-P liquid in the case of high S content, 8–24 wt% (Tsuno and Dasgupta, 2015; Li et al., 2016). In the Fe-Ni-C-S system, the carbon concentration would be reduced about half in the melts with $Xs = 0.1$ (6 wt% sulfur) (Zhang et al., 2018). S mainly occurs as FeS with Fe under lunar core pressure conditions (Hsieh et al., 1987). If we assume that Fe_3C is similar to Fe_3P bound in the liquid, the addition of FeS bond will replace Fe_3P. It is easy to explain the increase of $D^{SM/LM}_{p}$ along with increasing of S content (Fig. 7, Righter and Drake, 2000).

If we assume that lunar core is fully crystallized and the core is composed by solid iron and some light elements. The main light element should be carbon, with the concentration of ~1.2 wt% (Righter et al., 2017). Sulfur content should be less than ~0.02 wt% due to the extremely low-solubility in solid iron at lunar core pressures (Li et al., 2001). According to the Fe-P phase diagram in this study, the bulk phosphorus budget in the lunar core could be around 0.85 ± 0.15 wt% if phosphorus is saturated in the core. Considering the integrate influence from nickel and carbon, the phosphorus solubility in the core should be less than 0.4 ± 0.1 wt% ($0.5 \times$ P loss). It is a little close to the modeled bulk P storage in the core by core-mantle differentiation, using the BSE-like P content (82 ± 8 ppm, Wang et al., 2018) as C^{P}_{BM} (Fig. 8). However, because an inner core is expected for thermal-dynamical reasons (Wieczorek, 2006), and an estimated average core density is 5.2 ± 1.0 kg/cm^3, lunar core model favors a liquid outer core (Garcia et al., 2011). About 60% volume of the core is liquid as implied by reanalyzes of Apollo-era seismic data (Weber et al., 2011). Righter et al. (2017) suggested the possibility of a C and S-poor core (0.5 wt% C, and 0.375 wt% S) which is consistent with all available geochemical and geophysical data and provides a simple heat source and mechanism for a lunar core dynamo. The inner core can be extensive 75–80% volume crystallized at 1300 °C with a relatively thin fluid outer core (Righter et al., 2017). Phosphorus content model for the lunar core (Fig. 8) indicates that phosphorus concentration must be less than ~0.3 wt% in the most optimistic scenario. Lunar core light element composition model suggested by Righter et al. (2017) results in 3.8–11.8 wt% S in the outer core. Following the trend of $D^{SM/LM}_{p}$ in Fig. 7, we speculate that the possible $D^{SM/LM}_{p}$ at the S-bearing lunar outer core P-T conditions is 0.18 ± 0.02 (Fig. 7). Using the core radius and density model proved by Antonangeli et al. (2015), the liquid outer core contains 49% of total core mass. Therefore, with the mass balance between solid inner core and liquid outer core, the P concentration is 0.09 ± 0.01 wt% in inner core and 0.51 ± 0.01 wt% in outer core ($C^{P}_{core} = 0.3$ wt%).

5. CONCLUSIONS

This work provides particular information of Fe-P binary phase diagram at 3 GPa and up to 1600 °C. The low-P iron observed in this study gives a new insight to constrain the phosphorus budget in the lunar core. With increasing temperature, the P solubility in solid iron decreases to ~0.7 wt% at 1500 °C and 3 GPa. The partition coefficient model for phosphorus between the metal and silicate melt is a function of pressure, temperature, and oxygen fugacity and has been well investigated at lunar core conditions (Righter et al., 2009, 2010; Steenstra et al., 2016a, 2016b, 2017). But the P budget in the lunar core relies on the P content of bulk Moon. Assuming the C^{P}_{BM} is like the P content of bulk silicate Earth, it would result in less than 0.3 wt % P in the lunar core. This relative low concentration is in agreement with an S- and C-poor core model suggested by Righter et al. (2017). Because of the complex composition model (Fe-Ni-C-S) for lunar core, the C^{P}_{core} should be smaller than the examined P solubility in the iron in this study. In the case of a full-crystallized core, the P core storage is expected less than ~0.4 wt% due to the negative effect caused by nickel and carbon. The $D_{p}^{SM/LM}$ is also determined as 0.10 ± 0.03 at 3 GPa and 1250–1550 °C in the Fe-P binary system with S-free. If the sulfur is taken into account, $D_{p}^{SM/LM}$ increases to 0.18 ± 0.02. In a scenario of solid inner core and liquid outer core, the P concentration is estimated as 0.09 ± 0.01 wt% in inner core and 0.51 ± 0.01 wt% in outer core. To be compatible with the lunar mantle or bulk silicate Moon abundance of P, the core should be P-poor although the phosphorus has high solubility (~10 wt%) in the liquid metal. Future works are needed to consider the maximum solubility of P in a complex system at lunar core conditions. We also note that titanium affects Fe-P bond in γ-iron (Kaneko et al., 1965), and there is perhaps an ilmenite-rich layer beyond lunar outer core (de Vries et al., 2010; Matsumoto et al., 2015). It is necessary to investigate the effect of titanium on the phosphorus partitioning in the lunar magma ocean.

ACKNOWLEDGEMENT

We thank Prof. Xiangping Gu for the help of micro-focused X-ray analyses. We are grateful to Dr. Wen Liang and Prof. Baohua Zhang for helpful discussions. The manuscript was improved by Dr. Terry Mernagh. This work was financially supported by the National Natural Science Foundation of China (Grant No. 41873073), the Western Light Talents Training Program of Chinese Academy of Sciences, and the Science and Technology Department of Guizhou Province (Grant Nos. [2015] 2140 and [2016] 1157).

APPENDIX A. SUPPLEMENTARY MATERIAL

Supplementary data to this article can be found online at https://doi.org/10.1016/j.gca.2019.03.037.

REFERENCES

Acet M., Herper H., Entel P. and Wassermann E. F. (2001) The phase stability of ε-Fe alloys. *J. Phys. IV France* **11**, 229–234.

Allègre C. J., Poirier J.-P., Humler E. and Hofmann A. W. (1995) The chemical composition of the Earth. *Earth Planet. Sci. Lett.* **134**, 515–526.

Antonangeli D., Morard G., Schmerr N. C., Komabayashi T., Krisch M., Fiquet G. and Fei Y. (2015) Toward a mineral physics reference model for the Moon's core. *Proc. Natl. Acad. Sci.* **112**, 3916–3919.

Armstrong J. T. (1995) CITZAF: a package of correction programs for the quantitative electron microbeam X-ray-analysis of thick polished materials, thin-films, and particles. *Microbeam Anal.* **4**, 177–200.

Baker H. (1992) *ASM Handbook: Alloy Phase Diagrams*. ASM Int., Mateirals Park, Ohio.

Bombardieri D. J., Norman M. D., Kamenetsky V. S. and Danyushevsky L. V. (2005) Major element and primary sulfur concentrations in Apollo 12 mare basalts: The view from melt inclusions. *Meteorit Planet Sci.* **40**, 679–693.

Bose K. and Ganguly J. (1995) Quartz-coesite transition revisited: Reversed experimental determination at 500–1200 °C and retrieved thermochemical properties. *Am. Mineral.* **80**, 231–238.

Chacko S. and De Bremaecker J. C. (1982) The evolution of the moon: A finite element approach. *Moon Planets* **27**, 467–492.

Chantel J., Jing Z., Xu M., Yu T. and Wang Y. (2018) Pressure dependence of the liquidus and solidus temperatures in the Fe-P binary system determined by in situ ultrasonics: implications to the solidification of Fe-P liquids in planetary cores. *J. Geophys. Res. Planets* **123**, 1113–1124.

Dasgupta R., Buono A., Whelan G. and Walker D. (2009) High-pressure melting relations in Fe-C-S systems: Implications for formation, evolution, and structure of metallic cores in planetary bodies. *Geochim. Cosmochim. Acta* **73**, 6678–6691.

Dasgupta R. and Walker D. (2008) Carbon solubility in core melts in a shallow magma ocean environment and distribution of carbon between the Earth's core and the mantle. *Geochim. Cosmochim. Acta* **72**, 4627–4641.

Dauphas N., Burkhardt C., Warren P. H. and Fang-Zhen T. (2014) Geochemical arguments for an Earth-like Moon-forming impactor. *Philos. Trans. R. Soc. A Math. Phys Eng. Sci.* **372**, 20130244.

Dera P., Lavina B., Borkowski L. A., Prakapenka V. B., Sutton S. R., Rivers M. L., Downs R. T., Boctor N. Z. and Prewitt C. T. (2008) High–pressure polymorphism of Fe_2P and its implications for meteorites and Earth's core. *Geophys. Res. Lett.* **35** (2008), 1–6.

de Vries J., van den Berg A. and van Westrenen W. (2010) Formation and evolution of a lunar core from ilmenite-rich magma ocean cumulates. *Earth Planet. Sci. Lett.* **292**, 139–147.

Ding S., Hough T. and Dasgupta R. (2017) New high pressure experiments on sulfide saturation of high-FeO* basalts with variable TiO_2 contents-implications for the sulfur inventory of the lunar interior. *Geochim. Cosmochim. Acta* **222**, 319–339.

Drake M. J. (1987) Siderophile elements in planetary mantles and the origin of the Moon. *J. Geophys. Res.* **92**, E377–E386.

Elkins-Tanton L. T., Burgess S. and Yin Q.-Z. (2011) The lunar magma ocean: Reconciling the solidification process with lunar petrology and geochronology. *Earth Planet. Sci. Lett.* **304**, 326–336.

Fei Y., Bertka C. M. and Finger L. W. (1997) High-pressure iron-sulfur compound, Fe_3S_2, and melting relations in the Fe-FeS system. *Science* **275**, 1621–1623.

Fei Y. and Brosh E. (2014) Experimental study and thermodynamic calculations of phase relations in the Fe-C system at high pressure. *Earth Planet. Sci. Lett.* **408**, 155–162.

Fei Y., Li J., Bertka C. M. and Prewitt C. T. (2000) Structure type and bulk modulus of Fe_3S, a new iron-sulfur compound. *Am. Mineral.* **85**, 1830–1833.

Fisher W. A., Lorenz K., Fabritius H., Hoffmann A. and Kalwa G. (1966) Investigations of phse transformations in pure iron alloys with a magnetic-balance. *Arch. Eisenhuttenwes.* **37**, 79–86.

Garcia R. F., Gagnepain-Beyneix J., Chevrot S. and Lognonné P. (2011) Very preliminary reference Moon model. *Phys. Earth Planet. Inter.* **188**, 96–113.

Gu T., Fei Y., Wu X. and Qin S. (2014) High–pressure behavior of Fe_3P and the role of phosphorus in planetary cores. *Earth Planet. Sci. Lett.* **390**, 296–303.

Gu T., Wu X., Qin S. and Dubrovinsky L. (2011) In situ high-pressure study of FeP: Implications for planetary cores. *Phys. Earth Planet. Inter.* **184**, 154–159.

Halliday A. N. and Wood B. J. (2010) The composition and major reservoirs of the Earth around the time of the Moon-forming giant impact. In *Treatise on Geophysics, volume 9: Evolution of the Earth* (ed. D. Stevenson). Elsevier, Amsterdam, pp. 13–50.

Haughton J. L. (1927) Alloys of iron research. Part VIII. The constitution of alloys of iron and phosphorus. *J. Iron Steel Inst.* **115**, 417–433.

Hauri E. H., Saal A. E., Rutherford M. J. and Van Orman J. A. (2015) Water in the Moon's interior: truth and consequences. *Earth Planet. Sci. Lett.* **409**, 252–264.

Hirayama Y., Fujii T. and Kurita K. (1993) The melting relation of the system, iron and carbon at high pressure and its bearing on the early stage of the Earth. *Geophys. Res. Lett.* **20**, 2095–2098.

Hsieh K. C., Vlach K. C. and Chang Y. (1987) The Fe-Ni-S system. I. A thermodynamic analysis of the phase equilibria and calculation of the phase diagram from 1173 to 1623 K. *High Temp. Sci.* **23**, 17–38.

Jana D. and Walker D. (1997) The impact of carbon on element during core formation. *Geochim. Cosmochim. Acta* **61**, 2759–2763.

Jing Z., Wang Y., Kono Y., Yu T., Sakamaki T., Park C., Rivers M. L., Sutton S. R. and Shen G. (2014) Sound velocity of Fe-S liquids at high pressure: Implications for the Moon's molten outer core. *Earth Planet. Sci. Lett.* **396**, 78–87.

Kaneko H., Nishizawa T., Tamaki K. and Tanifuji A. (1965) Solubility of phosphorus in α and γ-iron. *J. Japan Inst. Met.* **29**, 166–170.

Konostantinow N. (1910) Phosphide of iron. *Z. Anorg. Chem.* **66**, 209–227.

Kuskov O. L. and Kronrod V. A. (1998) Constitution of the Moon 5. Constraints on composition, density, temperature, and radius of a core. *Phys. Earth Planet Inter.* **107**, 285–306.

Kuwabara S., Terasaki H., Nishida K., Shimoyama Y., Takubo Y., Higo Y., Shibazaki Y., Urakawa S., Uesugi K., Takeuchi A. and Kondo T. (2016) Sound velocity and elastic properties of Fe-Ni and Fe-Ni-C liquids at high pressure. *Phys. Chem. Miner.* **43**, 229–236.

Laneuville M., Wieczorek M. A., Breuer D., Aubert J., Morard G. and Rückriemen T. (2014) A long-lived lunar dynamo powered by core crystallization. *Earth Planet. Sci. Lett.* **401**, 251–260.

Li J., Fei Y., Mao H. K., Hirose K. and Shieh S. R. (2001) Sulfur in the Earth's inner core. *Earth Planet. Sci. Lett.* **193**, 509–514.

Li Y., Dasgupta R., Tsuno K., Monteleone B. and Shimizu N. (2016) Carbon and sulfur budget of the silicate Earth explained by accretion of differentiated planetary embryos. *Nat. Geosci.* **9**, 781–785.

Liu L. G. and Bassett W. A. (1975) The melting of iron up to 200 kbar. *J. Geophys. Res.* **80**, 3777–3782.

Lognonné P. and Johnson C. L. (2007) Planetary seismology. In *Treatise in Geophysics* (ed. G. Schubert). Esevier, Oxford, U. K., pp. 69–122.

Lorenz K. and Fabritius H. (1962) Use of a magnetic balance for determination of phase diagrams in the solid start region of iron-rich systems. Investigation of the system iron-phosphorus. *Arch. Eisenhuttenwes.* **33**, 269–275.

Matsumoto K., Yamada R., Kikuchi F., Kamata S., Ishihara Y., Iwata T., Hanada H. and Sasaki S. (2015) Internal structure of the Moon inferred from Apollo seismic data and selenodetic data from GRAIL and LLR. *Geophys. Res. Lett.* **42**, 7351–7358.

McDonough W. F. (2003) Compositional model for the earth's core. In *Treatise on Geochemistry* (eds. K. K. Turekian and H. D. Holland). Elsevier Ltd., pp. 547–568.

Nakamura Y., Lammlein D., Latham G., Ewing M., Dorman J., Press F. and Toksöz N. (1973) New seismic data on the state of the deep lunar interior. *Science* **181**, 49–51.

Okamoto H. (1990) The Fe-P (iron-phosphorus) system. *Bull. Alloy Phase Diagr.* **11**, 404–412.

O'Neill H. S. C. (1991) The origin of the moon and the early history of the earth-A chemical model. Part 1: The moon. *Geochim. Cosmochim. Acta* **55**, 1135–1157.

Pepperhoff W. and Acet M. (2001) *Constitution and Magnetism of Iron and its Alloys*. Springer Engineering Materials. Springer-Verlag, Berlin Heidelberg, pp. 3–84.

Perrot P., Batista S. and Xing X. (2002) Assessed phase diagram of the Fe-P binary system: Datasheet from MSI Eureka in SpringerMaterials. In *Springer Materials* (ed. G. Effenberg). Springer-Verlag GmbH, Heidelberg.

Rai N. and van Westrenen W. (2014) Lunar core formation: new constraints from metal-silicate partitioning of siderophile elements. *Earth Planet. Sci. Lett.* **388**, 343–352.

Righter K. (2002) Does the Moon have a metallic core? Constraints from giant impact modeling and siderophile elements. *Icarus* **158**, 1–13.

Righter K. (2003) Metal-silicate partitioning of siderophile elements and core formation in the early Earth. *Annu. Rev. Earth Planet. Sci.* **31**, 135–174.

Righter K. (2011) Prediction of metal-silicate partition coefficients for siderophile elements: An update and assessment of PT conditions for metal-silicate equilibrium during accretion of the Earth. *Earth Planet. Sci. Lett.* **304**, 158–167.

Righter K. and Drake M. J. (1996) Core formation in earth's moon, mars, and vesta. *Icarus* **124**, 513–529.

Righter K. and Drake M. J. (2000) Metal/silicate equilibrium in the early earth-new constraints from the volatile moderately siderophile elements Ga, Cu, P, and Sn. *Geochim. Cosmochim. Acta* **64**, 3581–3597.

Righter K., Go B. M., Pando K. A., Danielson L., Ross D. K., Rahman Z. and Keller L. P. (2017) Phase equilibria of a low S and C lunar core: Implications for an early lunar dynamo and physical state of the current core. *Earth Planet. Sci. Lett.* **463**, 323–332.

Righter K., Humayun M., Campbell A. J., Danielson L., Hill D. and Drake M. J. (2009) Experimental studies of metal-silicate partitioning of Sb: Implications for the terrestrial and lunar mantles. *Geochim. Cosmochim. Acta* **73**, 1487–1504.

Righter K., Pando K. M., Danielson L. and Lee C. T. (2010) Partitioning of Mo, P and other siderophile elements (Cu, Ga, Sn, Ni Co, Cr, Mn, V, and W) between metal and silicate melt as a function of temperature and silicate melt composition. *Earth Planet. Sci. Lett.* **291**, 1–9.

Ringwood A. E. (1991) Phase transformations and their bearing on the constitution and dynamics of the mantle. *Geochim. Cosmochim. Acta* **55**, 2083–2110.

Roquet P. and Jegaden G. (1951) Contribution to the study of iron-phosphorus phase diagram. *Rev. Metall.* **48**, 712–721.

Rybacki E., Renner J., Konrad K., Harbott W., Runmmel F. and Stockhert B. (1998) A servohydraulically-controlled deformation apparatus for rock deformation under conditions of ultra-

high pressure metamorphism. *Pure Appl. Geophys.* **152**, 579–606.

Saklatwalla B. (1908) Constitution of iron and phosphorus compounds. *J. Iron Steel Inst.* **77**, 92–103.

Scheinberg A., Soderlund K. M. and Schubert G. (2015) Magnetic field generation in the lunar core: The role of inner core growth. *Icarus* **254**, 62–71.

Scott H. P., Huggins S., Frank M. R., Maglio S. J., Martin C. D., Meng Y., Santillán J. and Williams Q. (2007) Equation of state and high–pressure stability of Fe_3P–schreibersite: Implications for phosphorus storage in planetary cores. *Geophys. Res. Lett.* **34**, L06302.

Scott H., Kiefer B., Martin C. D., Boateng N., Frank M. and Meng Y. (2008) P-V equation of state for Fe_2P and pressure–induced phase transition in Fe_3P. *High Pressure Res.* **28**, 375–384.

Sha L. K. (2000) Whitlockite solubility in silicate melts: some insights into lunar and planetary evolution. *Geochim. Cosmochim. Acta* **64**, 3217–3236.

Spohn T., Konrad W., Breuer D. and Ziethe R. (2001) The longevity of lunar volcanism: implications of thermal evolution calculations with 2D and 3D mantle convection models. *Icarus* **149**, 54–65.

Steenstra E. S., Lin Y., Rai N., Jansen M. and van Westrenen W. (2017) Carbon as the dominant light element in the lunar core. *Am. Mineral.* **102**, 92–97.

Steenstra E. S., Rai N. and Van Westrenen W. (2015) New geochemical models of core formation in the moon from metal-silicate partitioning of 14 siderophile and chalcophile elements. In 46th Lunar Planet. Sci.Conf., pp. 1490.

Steenstra E. S., Rai N., Knibbe J. S., Lin Y. H. and van Westrenen W. (2016a) New geochemical models of core formation in the Moon from metal-silicate partitioning of 15 siderophile elements. *Earth Planet. Sci. Lett.* **441**, 1–9.

Steenstra E. S., Knibbe J. S., Rai N. and van Westrenen W. (2016b) Constraints on core formation in Vesta from metal–silicate partitioning of siderophile elements. *Geochim. Cosmochim. Acta* **177**, 48–61.

Steenstra E. S., Seegers A. X., Eising J., Tomassen B. G. J., Webers F. P. F., Berndt J., Klemme S., Matveev S. and van Westrenen W. (2018) Evidence for a sulfur-undersaturated lunar interior from the solubility of sulfur in lunar melts and sulfide-silicate partitioning of siderophile elements. *Geochim. Cosmochim. Acta* **231**, 130–156.

Stewart A. J. and Schmidt M. W. (2007) Sulfur and phosphorus in the Earth's core: The Fe-P-S system at 23 GPa. *Geophys. Res. Lett.* **34**, L13201.

Stewart A. J., van Westrenen W., Schmidt M. W. and Günther D. (2009) Minor element partitioning between fcc Fe metal and Fe-S liquid at high pressure: The role of crystal lattice strain. *Earth Planet. Sci. Lett.* **284**, 302–309.

Taylor G. J. and Wieczorek M. A. (2014) Lunar bulk chemical composition: A post-gravity recovery and interior laboratory reassessment. *Philos. Trans. R. Soc. A Math. Phys Eng. Sci.* **372**, 20130242.

Togashi S., Kita N. T., Tomiya A. and Morishita Y. (2017) Magmatic evolution of lunar highland rocks estimated from trace elements in plagioclase: A new bulk silicate Moon model with sub-chondritic Ti/Ba, Sr/Ba, and Sr/Al ratios. *Geochim. Cosmochim. Acta* **210**, 152–183.

Tsuno K. and Dasgupta R. (2015) Fe-Ni-Cu-C-S phase relations at high pressures and temperatures - the role of sulfur in carbon storage and diamond stability at mid- to deep-upper mantle. *Earth Planet. Sci. Lett.* **412**, 132–142.

Tsymbulov L. B. and Tsemekhman L. S. (2001) Solubility of carbon in sulfide melts of the system Fe-Ni-S. *Russ. J. Appl. Chem.* **74**, 925–929.

Uhlig H. H. (1954) Contribution of metallurgy to the origin of meteorites: part 1-structure of metallic meteorites, their composition and the effect of pressures. *Geochim. Cosmochim. Acta* **6**, 282–301.

Usselman T. M. (1975) Experimental approach to the state of the core; Part I, The liquidus relations of the Fe-rich portion of the Fe-Ni-S system from 30 to 100 kb. *Am. J. Sci.* **275**, 278–290.

Vogel R. (1929) On the system iron-phosphorus-carbon. *Arch. Eisenhuttenwes.* **2**, 449–456.

Wang H. S., Lineweaver C. H. and Ireland T. R. (2018) The elemental abundances (with uncertainties) of the most Earth-like planet. *Icarus* **299**, 460–474.

Weber R. C., Lin P. Y., Garnero E. J., Williams Q. and Lognonne P. (2011) Seismic detection of the lunar core. *Science* **331**, 309–312.

Wetzel D. T., Hauri E. H., Saal A. E. and Rutherford M. J. (2015) Carbon content and degassing history of the lunar volcanic glasses. *Nat. Geosci.* **8**, 755–758.

Wieczorek M. A. (2006) The constitution and structure of the lunar interior. *Rev. Mineral. Geochem.* **60**, 221–364.

Williams J. G., Boggs D. H., Yoder C. F., Ratcliff J. T. and Dickey J. O. (2001) Lunar rotational dissipation in solid body and molten core. *J. Geophys. Res. Planets* **106**, 27933–27968.

Williams J. G., Konopliv A. S., Boggs D. H., Park R. S., Yuan D. N., Lemoine F. G., Goossens S., Mazarico E., Nimmo F., Weber R. C., Asmar S. W., Melosh J., Neumann G. A., Philips R. J., Smith D. E., Solomon S. C., Watkins M. M., Wieczorek M. A., Andrews-Hanna J. C., Head J. W., Kiefer W. S., Matsuyama I., McGovern P. J., Taylor G. J. and Zuber M. T. (2014) Lunar interior properties from the GRAIL mission. *J. Geophys. Res. Planets* **119**, 1546–1578.

Zaitsev A. I., Dobrokhotova Z. V., Litvina A. D. and Mogutnov B. M. (1995) Thermodynamic properties and phase equilibria in the Fe-P system. *J. Chem. Soc. Faraday Trans.* **91**, 703–712.

Ziethe R., Seiferlin K. and Hiesinger H. (2009) Duration and extent of lunar volcanism: Comparison of 3D convection models to mare basalt ages. *Planet. Space Sci.* **57**, 784–796.

Zhang J., Dauphas N., Davis A. M., Leya I. and Fedkin A. (2012) The proto-Earth as a significant source of lunar material. *Nat. Geosci.* **5**, 251–255.

Zhang N., Parmentier E. M. and Liang Y. (2013) A 3-D numerical study of the thermal evolution of the Moon after cumulate mantle overturn: The importance of rheology and core solidification. *J. Geophys. Res. Planets* **118**, 1789–1804.

Zhang Z., Hastings P., Von der Handt A. and Hirschmann M. M. (2018) Experimental determination of carbon solubility in Fe-Ni-S melts. *Geochim. Cosmochim. Acta* **225**, 66–79.

Associate editor: Andrew J. Campbell